https://doi.org/10.5194/wes-2025-65
Preprint. Discussion started: 15 April 2025

eawe european academy of wind energy
Open Access WIND ENERGY SCIENCE DISCUSSIONS

Experimental study of transonic flow over a wind turbine airfoil

Abhyuday Aditya[1], Delphine De Tavernier[1], Ferdinand Schrijer[1], Bas van Oudheusden[1], and Dominic von Terzi[1]

[1]Faculty of Aerospace Engineering, Delft University of Technology, 2629HS Delft, The Netherlands

Correspondence: Abhyuday Aditya (a.aditya@tudelft.nl)

Abstract. For the largest wind turbines currently being designed, operation at cutout conditions can lead to the tip airfoil experiencing transonic flow conditions. To date, this phenomenon has primarily been explored through numerical simulations, but modelling uncertainties limits the reliability of these predictions. In response to this challenge, our study marks the first experimental investigation of a wind turbine airfoil under transonic conditions, for which we consider the FFA-W3-211 airfoil. Measurements are conducted in the high-subsonic range (Mach 0.5 and 0.6), utilizing Schlieren visualization and Particle Image Velocimetry (PIV) to characterise the airfoil across a range of angles of attack expected at cutout conditions. Unsteady shock wave formation is observed for the higher Mach number, with the shock oscillation range increasing with steeper angles of attack. Also, it is found that the presence of a local supersonic flow region does not consistently result in a shock wave. Our findings reveal that while calculations based on isentropic flow theory are reasonably effective in predicting the onset of transonic flow, they fail to predict the intensity of transonic flow effects, in particular, the formation and unsteady nature of shock waves. This underscores the need for higher-fidelity tools and experiments to capture the dynamic transonic flow effects on wind turbine airfoils.

1 Introduction

To meet the growing global demand for energy by environmentally sustainable means, wind turbines have been progressively increasing in size, enabling them to better capture the energy potential in the wind (Mehta et al., 2024a). This expansion is driven by the need to optimize energy generation to meet market needs (Mehta et al., 2024b). As a result, the next generation of offshore wind turbines is poised to feature rotor diameters of the order of 280 m, seen in the IEA 22MW reference wind turbine (RWT) design (Zahle et al., 2024). However, this increase in scale presents a series of unprecedented aerodynamic challenges that require new approaches and solutions in wind turbine design.

For example, the IEA 22MW RWT is designed to operate with blade tip speeds of up to 105 m/s. When this high rotational speed combines with a cut-out wind speed of approximately 25 m/s, the flow experienced by the tip airfoil surpasses a Mach number of 0.3. This is a critical threshold, as it suggests that for future turbines with even larger dimensions and higher tip speeds, the longstanding assumption of incompressible flow in aerodynamic modelling may no longer be applicable. This change in aerodynamic conditions requires a re-evaluation of design strategies to include the effects of compressibility, which can have significant implications for the performance and durability of wind turbines.

https://doi.org/10.5194/wes-2025-65
Preprint. Discussion started: 15 April 2025

eawe european academy of wind energy
Open Access WIND ENERGY SCIENCE DISCUSSIONS

Compressibility in airflow can introduce complex physical phenomena such as shock waves, which can adversely affect the turbine's efficiency and structural integrity. Despite the importance of understanding these effects, there has been limited research specifically addressing the occurrence of high-speed flow characteristics, such as shock waves, in wind turbine operations. One of the few studies that explored these dynamics was conducted by Wood (1997), who examined small horizontal axis wind turbines equipped with NACA0012 airfoils. This study aimed to investigate the possibility of utilizing shock-induced separation at the blade tips as a means of overspeed protection. However, it is important to note that symmetric airfoils like the NACA0012 are not typically employed at the tips of utility-scale wind turbine blades, thus limiting the applicability of these findings to modern large-scale turbines.

Another notable study by Hossain et al. (2013) focused on the propagation of shock waves on the NREL Phase VI S809 wind turbine airfoil, employing 2D RANS simulations to analyze these effects at varying angles of attack. Nevertheless, the study was conducted at a free-stream Mach number of 0.8, a value that is currently considered well beyond the reach of existing and envisioned wind turbine designs. Thus, while informative, this research does not realistically address the conditions relevant to modern, large-scale wind turbines.

The presence of supersonic flow conditions in real-world, large-scale wind turbine operations remains an underexplored area. Only recently have wind turbines become large enough to approach tip speeds that result in Mach numbers nearing 0.3, thereby bringing compressibility effects into play. In offshore environments, where these large turbines are often deployed, dynamic factors such as free-stream turbulence, the aeroelastic response of blades, and the movement of floating platforms can further elevate the instantaneous wind speed encountered by the tip airfoil. Additionally, when operating at rated power levels close to cut-out conditions, the tip airfoils of these turbines may experience large negative angles of attack (AoAs). Research by De Tavernier and von Terzi (2022) and further confirmed by Vitulano et al. (2025) through URANS simulations demonstrated that even for the IEA 15MW RWT, which has a lower maximum rotor tip speed of 95 m/s compared to the 105 m/s of the IEA 22MW RWT, such conditions, combined with inflow turbulence, can generate a strong suction peak. This peak can drive the tip airfoil into a transonic flow regime, potentially leading to shock wave formation at the blade tip. This phenomenon is particularly concerning because shock waves can reduce aerodynamic performance and induce flow unsteadiness, which, coupled with flow separation, can result in a phenomenon known as transonic buffet. Extensively studied in supercritical airfoils D'Aguanno et al. (2021), transonic buffet can cause significant vibrations, posing a severe threat to the structural integrity and operational lifespan of wind turbine blades.

Although the implications of compressibility on wind turbine performance have previously been investigated, primarily through numerical simulations as detailed in studies such as Vitulano et al. (2025), there is a noticeable lack of reliable experimental data on the behavior of typical wind turbine airfoils operating within the compressible flow regime. Therefore, it is imperative to develop a deeper understanding of the specific conditions under which supersonic flow occurs on wind turbine airfoils and to determine if these conditions lead to the formation of shock waves. This study seeks to address this gap by focusing on the FFA-W3-211 airfoil, which is employed at the blade tips of both the IEA 15MW and 22MW reference wind turbines. By using experimental methods, this research aims to provide a detailed characterization of the flow dynamics of this airfoil under transonic conditions, to support the future design and operation of large-scale wind turbines.

https://doi.org/10.5194/wes-2025-65
Preprint. Discussion started: 15 April 2025

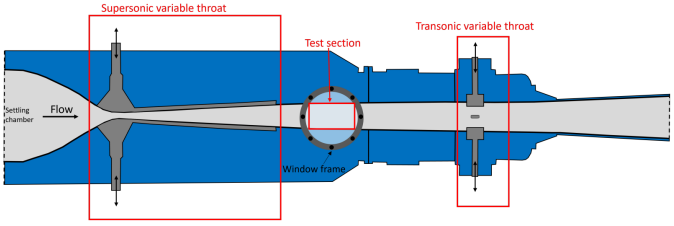

Figure 1. A schematic of the Transonic-Supersonic Wind Tunnel (TST-27) (D'Aguanno et al., 2021).

2 Methodology

2.1 Wind Tunnel Facility

Measurements on a static FFA-W3-211 airfoil have been performed in the TST-27 transonic-supersonic blowdown-type wind tunnel at the Delft University of Technology (Figure 1). In the transonic mode of operation, the free-stream Mach number in the test section is controlled by a choke mechanism downstream of it and can be varied in the range 0.5 ± 0.01 to 0.85 ± 0.01. The test section is 255 mm $\times$ 280 mm in height and width, respectively, with transparent windows for optical access present on both sidewalls. The total pressure in the tunnel can range from $1.5 - 4$ bar, which allows one to vary the Reynolds number for the same Mach number, and is set to $p_0 = 2$ bar in the current experiments, while the total temperature, which is not actively controlled, is $T_0 = 288$ K. For the current study, Mach numbers of 0.5 ± 0.01 and 0.6 ± 0.01 are considered, which correspond to free-stream velocities of 166 and 197 m/s, respectively.

2.2 Wind Tunnel Model

The tip airfoil used in the IEA 15MW and 22MW RWTs is the FFA-W3-211 (see Figure 2), belonging to the DTU FFA series (Bertagnolio et al., 2001). A model of the airfoil with a chord of 67 mm was used for the tests, with a thickness-to-chord ratio of 21%. The model spans the entire width of the test section, resulting in an aspect ratio of more than 4, to approach 2D aerodynamic behavior. At the maximum inclination of $10°$, the geometric blockage ratio is $\approx 6\%$. While testing in the wind tunnel, for convenience, the airfoil model is installed flipped upside-down compared to the conventional orientation that is depicted in Figure 2. However, the results presented in the paper maintain the conventional orientation. The AoA of the model is adjusted manually using a digital angle gauge with an uncertainty of $\pm 0.1°$, and the values reported throughout refer to the geometric AoA with respect to the conventional orientation, which would be different from the actual AoA in the test section due to wall interference effects on the streamline curvature.

2.3 Schlieren Imaging

Schlieren imaging maps the gradient of the refractivity of a medium, which can be interpreted as a visualization of gradients of density and is thus useful for identifying compressible flow features such as shock and expansion waves. For the current study, Schlieren is used as a preliminary analysis tool to identify conditions of particular interest that need to be investigated in

https://doi.org/10.5194/wes-2025-65
Preprint. Discussion started: 15 April 2025

eawe european academy of wind energy
Open Access WIND ENERGY SCIENCE DISCUSSIONS

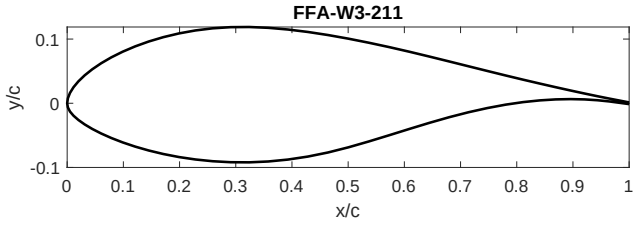

Figure 2. The FFA-W3-211 airfoil shape.

depth. A Z-type Schlieren setup is employed, using a white LED with a 1 mm diameter pinhole for illumination, and images are acquired at a rate of 100 Hz using a LaVision Imager sCMOS at a cropped resolution of 1920 $\times$ 1038 pixels, corresponding to a field of view of 112 mm $\times$ 61 mm in the streamwise and vertical extent. The exposure time is maintained at 9 μs in order to avoid blurring of the shock motion.

2.4 Particle Image Velocimetry

Particle Image Velocimetry (PIV) is used in a planar configuration to measure two components of the velocity field at the spanwise center of the airfoil model. Given the full-field and quantitative measurement capabilities of PIV, it is employed as the primary tool in this investigation to study the occurrence of transonic effects. For seeding the flow, DEHS (Di-Ethyl-Hexa-Sebacat) particles are used with an average diameter of 1 μm. For illuminating the particles, an Nd:YAG laser, with a wavelength of 532 nm, is shaped into a light sheet of approximately 1.5 mm thickness and projected along the spanwise center of the TST-27 test section, operating at a repetition rate of 15 Hz. Two LaVision Imager sCMOS cameras mounted with Nikon Nikkor 105 mm lenses are used with an f-stop of 8 on either side of the test section to acquire the particle images at an acquisition frequency of 15 Hz, with an overlap between the two fields-of-view that are combined later to create a total field-of-view covering $\sim$ 98 mm $\times$ 55 mm in the streamwise and transverse directions, respectively, at a scale of approximately 49 px/mm. This translates to a total field of view spanning 146 $\times$ 82 % of the chord. In total, 1200 snapshots are recorded for each configuration, to ensure enough instances for the convergence of flow statistics. The synchronization between the cameras and the laser is achieved using a LaVision Programmable Timing Unit (PTU) controlled by a PC using LaVision DaVis. The acquired raw images are then processed in LaVision DaVis to obtain the velocity field, which has a velocity vector pitch of 0.16 mm, in both streamwise and vertical directions. A schematic of the experimental setup is presented in Figure 3. Further post-processing of the velocity fields has been carried out using MATLAB.

2.5 Local Mach number calculations

Using the energy equation for adiabatic flow (i.e. the constant value of the total temperature), the local Mach number can be related to the local velocity magnitude, U, and the total temperature of the flow, T_0:

$$Ma = \frac{U}{\sqrt{\gamma R T_0 - \left(\frac{\gamma-1}{2}\right) U^2}} \tag{1}$$

https://doi.org/10.5194/wes-2025-65
Preprint. Discussion started: 15 April 2025

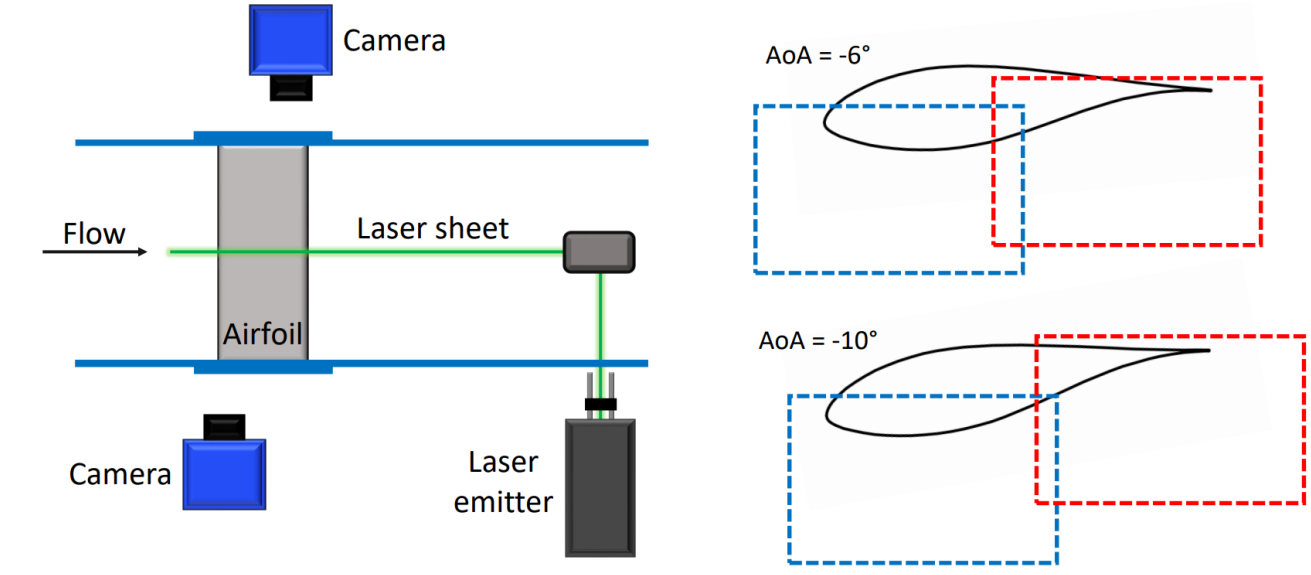

Figure 3. PIV setup details: cameras and laser arrangement around the test section (left) and approximate fields-of-view for two different inclinations (right).

The total temperature is determined as the temperature measured in the settling chamber of the TST-27 (see Figure 1), using a thermocouple with an accuracy of $\pm 1°$C. During the experiments, the measured total temperature varied in the range 15-17°C. The overall results were not found to be remarkably sensitive for small variations of the total temperatures in the given range, hence, an average value of $T_0 = 288$ K is used throughout. Since both streamwise and vertical velocity components are obtained from the post-processed PIV measurements, it is relatively straightforward to determine the local Mach numbers using equation 1.

2.6 Uncertainty Quantification

The experimental measurements are associated with several uncertainties, and these are estimated below.

Since the ensemble size used for calculating statistical quantities is finite, it leads to a statistical convergence uncertainty related to the mean and standard deviation estimates. This is quantified using the standard deviation, $\sigma_u = \sqrt{u'^2}$, and ensemble size, N, (Benedict and Gould, 1996) as:

$$\varepsilon_{\bar{u}} = \frac{\sigma_u}{\sqrt{N}} \tag{2}$$

And on the standard deviation itself:

$$\varepsilon_{\sigma_u} = \frac{\sigma_u}{\sqrt{2N}} \tag{3}$$

https://doi.org/10.5194/wes-2025-65
Preprint. Discussion started: 15 April 2025

eawe european academy of wind energy
Open Access WIND ENERGY SCIENCE DISCUSSIONS

Table 1. Sources of uncertainty.

Source	Value	Unit
Mean of total velocity, $\varepsilon_{\bar{U}}$	≤ 2.87	m/s
Standard deviation of total velocity, ε_{σ_U}	≤ 2.02	m/s
Mean of local Mach number, ε_{Ma}	≤ 0.01	-
Standard deviation of local Mach number, $\varepsilon_{\sigma_{Ma}}$	≤ 0.005	-
Cross-correlation, ε_{cc}	≤ 2.03	m/s
Spatial resolution, ε_{sr}	$\leq 1\%$	-

To estimate an upper limit to the statistical uncertainties, the maximum standard deviation value in the flow-field is used to calculate the same. In the current study, the acquisition rate (15 Hz) is sufficiently low to consider subsequent PIV snapshots as uncorrelated, which means that we can use the total number of snapshots, $N = 1200$, to calculate the statistical uncertainties.

Another uncertainty arises from the cross-correlation procedure employed to calculate velocities from the particle image pairs. For planar PIV, the uncertainty, ε_{corr}, is estimated to be 0.1 pixels. It can be further translated in terms of uncertainty in instantaneous velocity as (Humble, 2009):

$$\varepsilon_{cc} = \frac{\varepsilon_{corr}}{M \cdot \delta t} \tag{4}$$

where $M = 0.32$ is the magnification in the current setup and δt is the laser pulse separation time.

Finally, the window size (WS) used for cross-correlation allows resolving flow structures up to a certain limit, which is represented by a wavelength λ. The resulting uncertainty is modelled using a sinc function, as shown by Schrijer and Scarano (2008).

$$\varepsilon_{sr} = \frac{u}{u_0} = \text{sinc}\left(\frac{WS}{\lambda}\right) \tag{5}$$

A multi-step correlation procedure, also employed in the current study, makes this uncertainty less pronounced. Also, given that the smallest resolvable flow structures are twice the window size (De Kat and Van Oudheusden, 2012), it is safe to approximate that $\epsilon_{sr} \leq 1\%$.

3 Experimental Design

In their study, De Tavernier and von Terzi (2022) calculated the envelope separating the subsonic regime and (local) supersonic flow regime in terms of the critical pressure coefficient, $C_{p,cr}$, and the free-stream Mach number, Ma_∞, employing isentropic compressible flow theory (in combination with the Prandtl-Glauert correction). This was translated into a combination of Ma_∞ and the AoA for the FFA-W3-211 airfoil with the help of XFoil simulations. With the help of this envelope, De Tavernier and von Terzi (2022) conducted simulations in OpenFAST which revealed that the IEA 15MW RWT, when operating near cut-off

https://doi.org/10.5194/wes-2025-65
Preprint. Discussion started: 15 April 2025

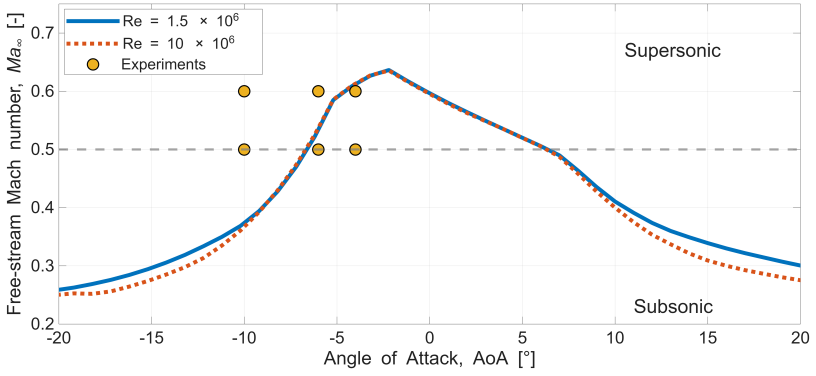

Figure 4. The transonic envelope showing the separation between complete subsonic flow and transonic flow for an FFA-W3-211 airfoil at different Reynolds numbers. Additionally, the horizontal dashed grey line shows the lower operation limit of TST-27 and the yellow markers indicate the experimental test conditions for the current investigation.

wind conditions at high free-stream turbulence levels, may encounter large negative angles of attack (in the order of $-10°$ to $-15°$) at moderately high subsonic free-stream Mach numbers (~ 0.3), thus pushing the tip airfoil intermittently into the transonic flow regime. The same transonic envelope calculations have been used to inform the experimental design of the current study, as shown in Figure 4.

The test conditions for conducting experiments are limited by the capabilities of the choke mechanism of the TST-27 wind tunnel which currently allows only for a minimum Ma_∞ of 0.5 in the test section, marked in Figure 4 with a horizontal black dashed line. Consequently, only two free-stream Mach numbers were tested, $Ma_\infty = 0.5$ and 0.6. While these free-stream Mach numbers are beyond the operational limits of current wind turbines, it is still useful to test at these conditions to validate the transonic envelope calculations in Figure 4 and to test the limits at which supersonic flow features like shock waves might occur. Three AoAs are chosen for each of the Mach numbers: $-4°$, $-6°$ and $-10°$. As mentioned, the geometric AoAs are reported here, without corrections for streamline curvature due to wall interference. Also, Ma_∞ reported here is not corrected for blockage effects resulting from the finite height of the test section and the presence of the model. This choice of Ma_∞ and AoA combinations allows for studying the transition from a complete subsonic regime to a transonic regime, through both an increase in the (negative) AoA, representing increased streamline curvature for the same free-stream conditions (e.g. going from $-6°$ to $-10°$ at $Ma_\infty = 0.5$), as well as an increase in free-stream Mach number for the same geometry (e.g. going from $Ma_\infty = 0.5$ to 0.6 at AoA$= -6°$).

There are several uncertainties involved in both: obtaining the transonic envelope and determining the exact conditions experienced by the model during experimental testing. The transonic envelope calculations rely on the isentropic flow theory, which simply predicts the onset of local supersonic flow without taking all viscous effects into account. Using XFoil to translate $C_{p,cr}$ vs Ma_∞ into Ma_∞ vs AoA resolves this limitation to some extent, but still without the reliable accuracy of higher-fidelity methods like RANS. Moreover, the compressibility corrections employed (Prandtl-Glauert) are also of low accuracy.

https://doi.org/10.5194/wes-2025-65
Preprint. Discussion started: 15 April 2025

eawe european academy of wind energy
Open Access WIND ENERGY SCIENCE DISCUSSIONS

Table 2. Experimental conditions.

Parameter	Value(s)	Unit
Free-stream Mach number (Ma_∞)	0.5 & 0.6	-
Free-stream velocity (U_∞)	166 & 197	m/s
Free-stream Mach number (corrected)	0.51 & 0.62	-
Chord-based Reynolds number (Re_c)	1.4×10^6 & 1.6×10^6	-
Total pressure (p_0)	2.0	bar
Total temperature (T_0)	288	K
Angle of Attack (AoA)	-4, -6 & -10	°
Model chord	67	mm
Model span	280	mm

Another noteworthy aspect of these calculations is their reliance on the Reynolds number. In Figure 4, the transonic envelopes are calculated for chord-based Reynolds numbers of 1.5×10^6 and 10×10^6. Based on these isentropic flow calculations, the deviation in the onset of transonic flow for different Reynolds numbers appears to be most pronounced at lower Mach numbers (< 0.5) in Figure 4. Furthermore, The work of Vitulano et al. (2025) using URANS simulations showed that the Reynolds number is an important parameter for determining the onset of transonic flow on the FFA-W3-211, possibly more important than suggested by the isentropic flow calculations presented in Figure 4. Particularly, a higher Reynolds number leads to an early onset of local supersonic flow pockets on the FFA-W3-211 for the same combination of Ma_∞ and AoA. It is important to note that a Reynolds number of the order of 10^7 is a more reasonable estimate for a full-scale wind turbine tip airfoil, where we expect transonic conditions to occur. However, the test facility utilized for the present study limits the Reynolds number achieved on the wind tunnel model to the order of 1.5×10^6 (see Table 2). Hence, we are unable to experimentally investigate the Reynolds number effect on the onset of transonic flow presently.

Inside the wind tunnel, the reported free-stream Mach number is expected to increase because of the presence of the model in the closed test section. Calculating the true Mach number experienced by the airfoil model due to the aforementioned blockage effect commonly involves a combination of potential flow theory and empiricism, and the method described by Herriot (1947) was used to calculate the corrected free-stream Mach numbers (see Table 2). The calculations show that the true Mach number in the presence of the model is estimated to be higher by a maximum of 3%. However, no corrections are made to determine the true AoA experienced by the model, which is expected to be slightly less steep compared to the geometric AoA due to the streamline curvature. These uncertainties associated with testing in a closed wind tunnel affect the flow-field by modifying the free-stream conditions. However, it is safe to assume that the physics is not drastically altered compared to what would be expected at the uncorrected conditions of Ma_∞ and AoA. Thus, the uncorrected Ma_∞ and geometric AoA are refered to throughout the text, assuming it deviates only slightly from the corrected conditions.

https://doi.org/10.5194/wes-2025-65
Preprint. Discussion started: 15 April 2025

4 Results

4.1 Local Mach Number Trends

In all the figures presented henceforth, the flow direction is from left to right.

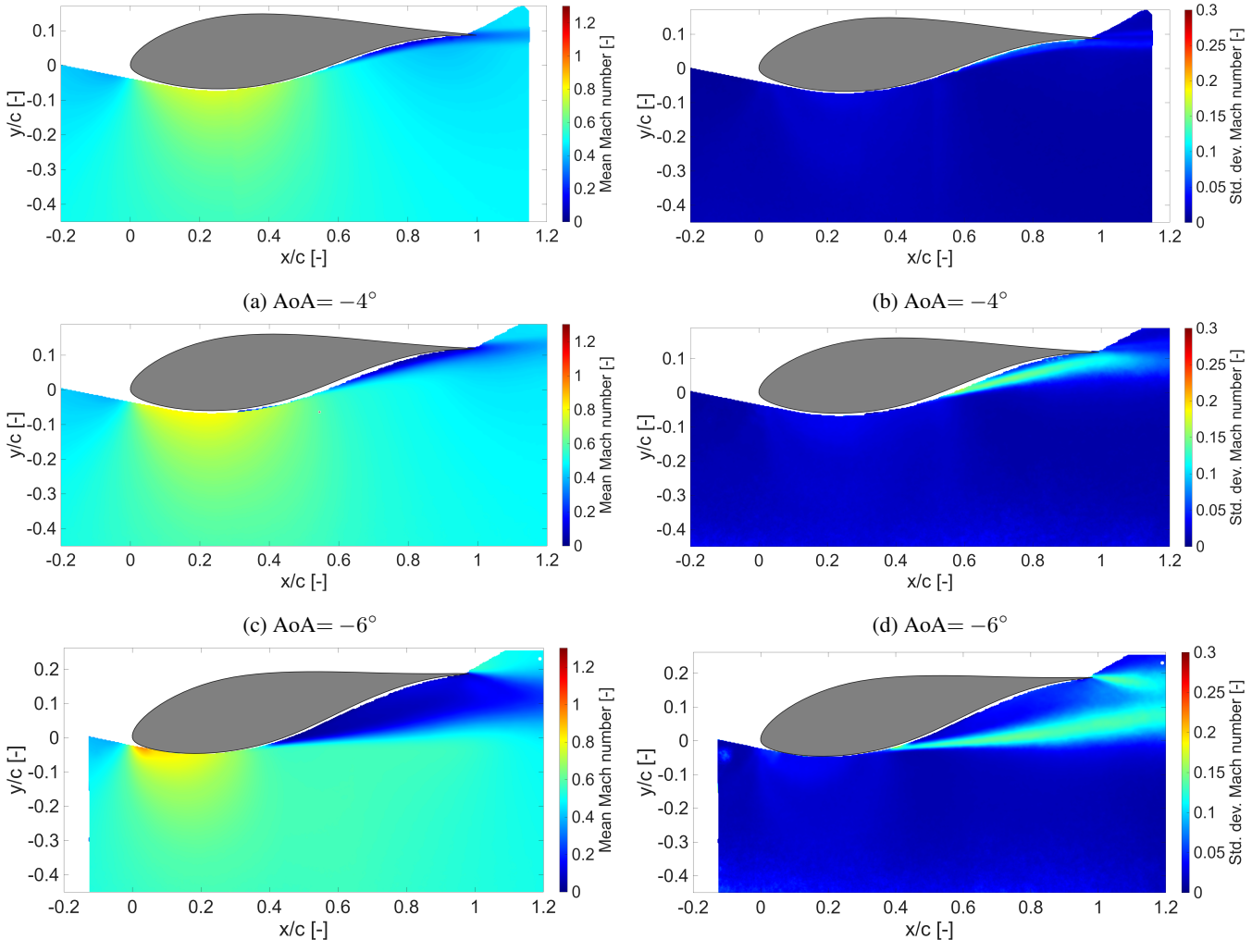

(a) AoA= $-4°$ (b) AoA= $-4°$

(c) AoA= $-6°$ (d) AoA= $-6°$

(e) AoA= $-10°$ (f) AoA= $-10°$

Figure 5. Contours of Mach number: mean values (left column) and standard deviation (right column) for $Ma_\infty = 0.5$.

The first set of cases is presented in Figure 5 for $Ma_\infty = 0.5$. The two shallower inclinations, i.e., AoA= $-4°$ and AoA= $-6°$, are predicted to be completely subsonic in Figure 4. As observed in the mean local Mach number for AoA= $-4°$, in Figure 5a, the maximum local Mach number achieved is 0.8. This occurs close to the airfoil surface around the maximum thickness location. A similar observation is also made for the mean local Mach number field for AoA= $-6°$, the main difference being

https://doi.org/10.5194/wes-2025-65
Preprint. Discussion started: 15 April 2025

eawe european academy of wind energy
Open Access WIND ENERGY SCIENCE DISCUSSIONS

that a larger extent of the flow now accelerates to the maximum local Mach number of 0.8, as shown in Figure 5c. Also, the flow is seen to accelerate quicker around the leading edge, which is explained by the higher suction peak resulting from the steeper inclination.

Following the same trend, the steepest inclination of AoA$= -10^\circ$ sees the flow at the leading edge accelerate very close to sonic conditions (local Mach number of 1) in the mean sense (Figure 5e). According to the transonic envelope predictions in Figure 4, an AoA of -10° at $Ma_\infty = 0.5$ lies deep within the transonic flow zone. However, the mean local Mach number field suggests only the probability of a tiny pocket of supersonic flow at the leading edge.

None of the above configurations are able to achieve consistent sonic conditions, which is clear from the standard deviation in the local Mach numbers. Close to the leading edge, the maximum standard deviation barely reaches 0.05 for the steepest inclination of -10° (Figure 5f. Combining this with the maximum mean local Mach number of around 1 at the same location, the flow can be accelerated intermittently to supersonic conditions for $Ma_\infty = 0.5$, AoA$= -10^\circ$. The occurrence of local supersonic flow in an instantaneous sense for this configuration is further investigated in section 4.2. For the other two cases, there is no indication of local supersonic flow based on the mean and standard deviation of the local Mach numbers.

As the inclination is steepened, a strongly fluctuating shear layer is seen to emerge in the flow. This is reflected in the standard deviation of the local Mach number for different inclinations. For AoA$= -6^\circ$, the fluctuating shear layer is suggested to start from $x/c \approx 0.5$ (Figure 5d); for the steeper AoA$= -10^\circ$, it starts more upstream at $x/c \approx 0.4$ (Figure 5f). This is indicative of the strong adverse pressure gradients developed downstream of the maximum thickness as the airfoil steepens, possibly resulting in flow separation.

In Figure 6, the mean and standard deviation of the local Mach number are presented for the higher free-stream Mach number of 0.6. A mean local Mach number equal to 1 is marked with a solid black line. Note that the contour scales are consistent across Figs. 5 and 6.

At first glance, the mean local Mach number reaches supersonic conditions for all AoAs, with the supersonic pocket increasing with steeper inclination. Furthermore, the start of the supersonic pocket consistently shifts closer to the leading edge as the AoA steepens. For AoA$= -4^\circ$, the supersonic flow pocket in the mean flow is small, extending from $x/c \approx 0.2 - 0.3$ up to $y/c \approx -0.1$ (Fig. 6a. The vertical extent of the local supersonic region grows to $y/c \approx -0.2$ for the steeper AoAs. For AoA$= -6^\circ$, the horizontal extent of the supersonic pocket is $x/c \approx 0.1 - 0.35$ (see Fig. 6c) and for $AoA = -10^\circ$, it is $x/c \approx 0 - 0.3$. These observations are consistent with expectations, given that a steeper AoA leads to a stronger suction peak at the airfoil leading edge.

In terms of the standard deviation of the local Mach number, it is again observed that the fluctuating shear layer grows stronger with steeper AoAs. Upon comparing Figs. 5 and 6, it is clear that a higher free-stream Mach number is seen to produce stronger fluctuations in the shear layer at the same AoA. Interestingly, a region of relatively high standard deviation (0.1-0.15) extending into the transverse direction is observed closer to the maximum thickness location for all configurations at $Ma_\infty = 0.6$, presented in Figs. 6b, 6d and 6f. Furthermore, the downstream edge of the local supersonic flow region coincides with the aforementioned transverse region of high standard deviation in the local Mach number.

https://doi.org/10.5194/wes-2025-65
Preprint. Discussion started: 15 April 2025

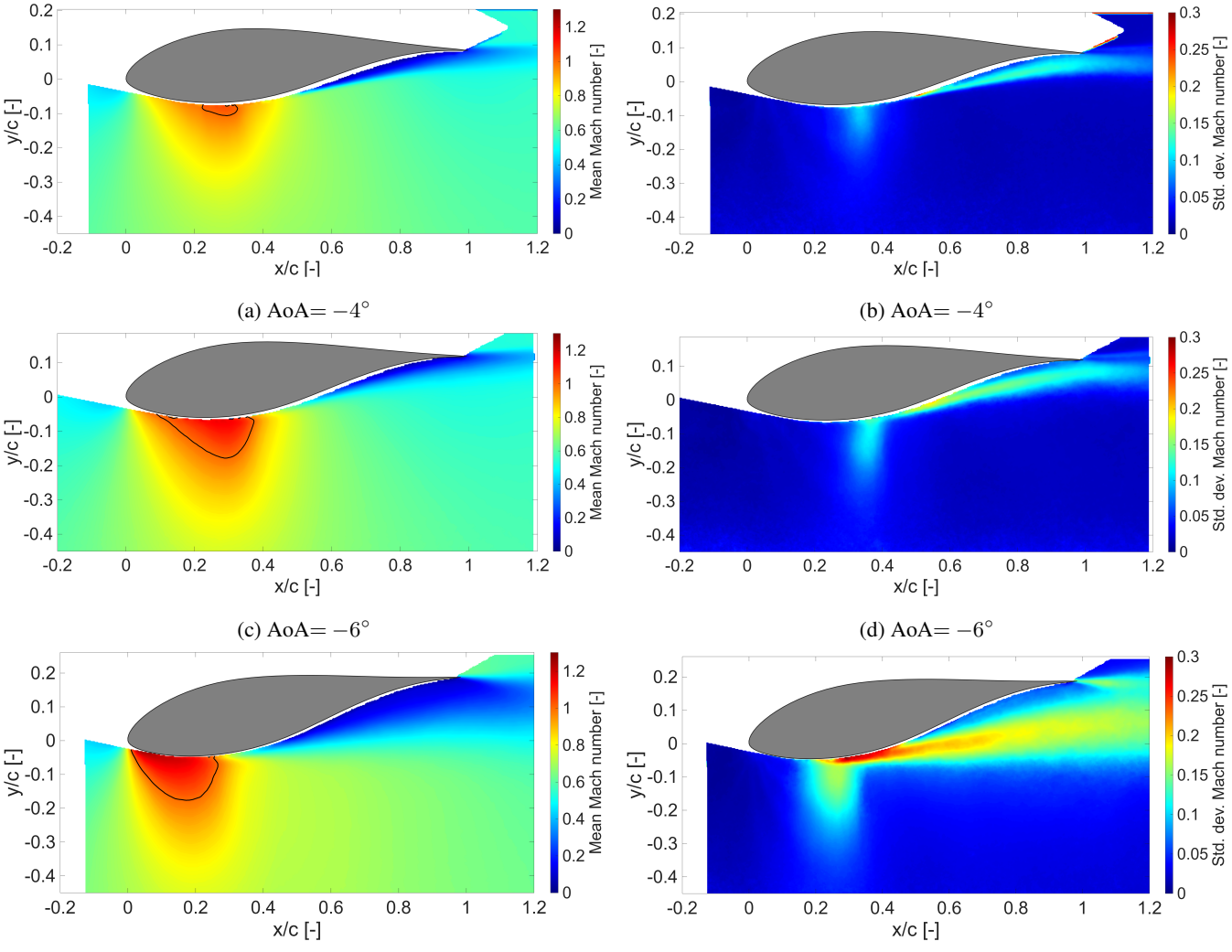

(a) AoA= -4° (b) AoA= -4°

(c) AoA= -6° (d) AoA= -6°

(e) AoA= -10° (f) AoA= -10°

Figure 6. Contours of Mach number: mean values (left column) and standard deviation (right column) for $Ma_\infty = 0.6$. The solid black line represents a local Mach number of 1.

For e.g., in Figure 6f, the standard deviation in the local Mach number is close to 0.15 in $x/c \approx 0.15-0.35$ up to $y/c \approx -0.2$ from the airfoil surface. In the same spatial extent, the mean local Mach number varies between 0.9 and 1.2, as shown in Figure 6e. Thus, at any instant, the local Mach number in the region could take a value between 0.75 and 1.35, suggesting the possibility of a moving shock wave. The presence of shock waves is investigated further in Section 4.3 by examining instantaneous Mach number contours.

Similar observations are made for the shallower AoAs of $= -6^\circ$ and -4° at $Ma_\infty = 0.6$. Both configurations exhibit regions where the instantaneous flow experiences subsonic and supersonic conditions intermittently, as deduced from the respective

https://doi.org/10.5194/wes-2025-65
Preprint. Discussion started: 15 April 2025

eawe european academy of wind energy
Open Access WIND ENERGY SCIENCE DISCUSSIONS

mean and standard deviation in local Mach numbers. At this point, it is useful to look back at the predictions of the transonic envelope calculations in Figure 4 for $Ma_\infty = 0.6$. For an AoA of $-4°$, the transonic envelope suggests that no local supersonic flow is to be expected. However, the measurements at this configuration prove otherwise; the mean flow has a supersonic region in Figure 6a, while the standard deviation in the local Mach number even suggests the possibility of unsteady shock waves. This serves to highlight the role of the uncertainties discussed in section 3. Either the actual transonic envelope is significantly lower (shifted down in terms of Ma_∞), or the free-stream Mach number experienced by the model is increased sufficiently due to blockage effects for AoA$= -4°$ at $Ma_\infty = 0.6$ to crossover into the transonic flow regime, or both.

4.2 Probability of Local Supersonic Flow

The mean local Mach number fields were analyzed along with the standard deviations in the previous section; however, they do not provide a complete picture of the instantaneous flow behaviour. To investigate flow intermittency in terms of supersonic flow, the probability of occurrence of supersonic conditions in the flowfield is calculated. This is simply given by the ratio of the number of snapshots with supersonic flow at a particular location to the total number of snapshots. The corresponding probability maps are presented in Figure 7. Note that two out of the six configurations tested did not experience local supersonic flow: AoA$= -4°$ and $-6°$ for $Ma_\infty = 0.5$; thus, those are not included in the current analysis.

For the shallowest AoA of $-4°$ at $Ma_\infty = 0.6$, the local flow becomes supersonic only in a small region, extending from $x/c \approx 0.2 - 0.35$. The dashed line denotes a 50% probability of the occurrence of supersonic flow, with higher probabilities inside the enclosed region. For this case, the maximum probability of local supersonic flow occurring is only $\approx 79\%$, which means no region of the flow is supersonic for more than 80% of the time. At steeper AoA for the same Ma_infty: $-6°$ and $-10°$, the probability maps show a more significant and consistent occurrence of supersonic flow. The region enclosing a minimum chance of 50% for the occurrence of supersonic flow is flatter (maximum $y/c \approx -0.18$) and more elongated (x/c ranging from 0.05 to 0.35) for AoA$= -6°$ (in Fig. 7b) as compared to AoA$= -10°$. For the latter, a 50% probability of supersonic flow occurs over $y/c \approx -0.2$ and $x/c \approx 0.02 - 0.25$, i.e. farther upstream as shown in Fig. 7c. It makes sense that we see such high probabilities of supersonic flow for the steeper AoAs since the mean flow also exhibits a significant region of local Mach numbers beyond 1 in both cases (AoA$= -6°$ and $-10°$), as seen in Figures 6c and 6e.

In Figure 7d, we observe that only a very small region near the airfoil leading edge (0-5% of the chord) appears to experience supersonic flow, only around 10-35% of the time. This corresponds to the steepest inclination of $-10°$ at $Ma_infty = 0.5$. Thus, the flow breaches local sonic conditions in an intermittent sense and only in a negligibly small region, compared to the configurations at $Ma_\infty = 0.6$. Likely, the pressure gradient is not strong enough to result in a flow acceleration sufficient for creating shock waves, and the flow might decelerate smoothly to subsonic conditions. Note that the scale extends to a maximum probability of only 0.35 in this case (Figure 7d), compared to a maximum of 1 in the other cases. It is evident that a drop in Ma_∞ from 0.6 to 0.5 drastically alters the flow behaviour for the same AoA of $-10°$, despite both conditions lying deep inside the predicted transonic regime according to the envelope calculations in Figure 4. Thus, this is an example where the actual flow behaviour is more complex than low-order transonic envelope calculations can envisage.

https://doi.org/10.5194/wes-2025-65
Preprint. Discussion started: 15 April 2025

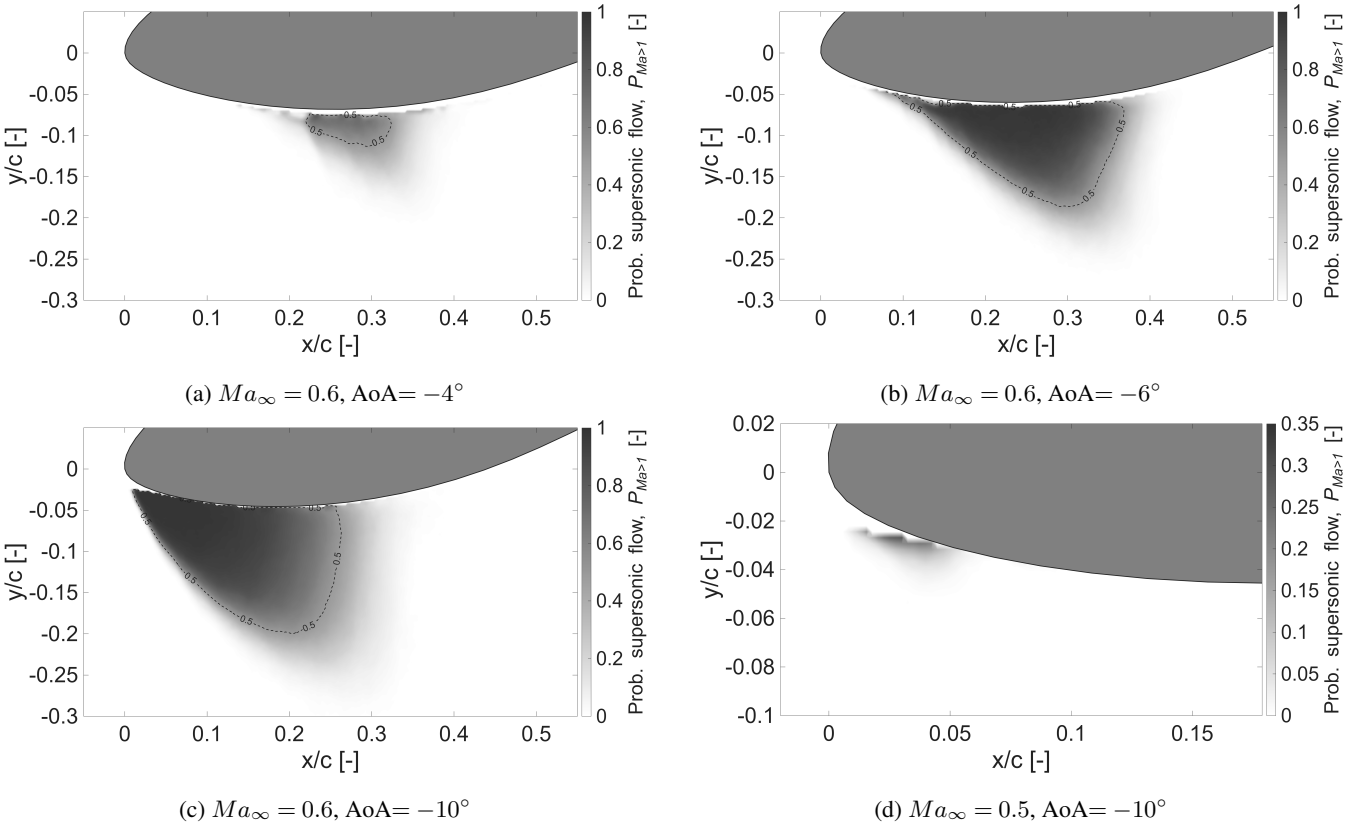

(a) $Ma_\infty = 0.6$, AoA$= -4°$

(b) $Ma_\infty = 0.6$, AoA$= -6°$

(c) $Ma_\infty = 0.6$, AoA$= -10°$

(d) $Ma_\infty = 0.5$, AoA$= -10°$

Figure 7. Distribution of the probability of supersonic flow for different cases. The contour corresponding to a probability of 0.5 is marked with a dashed line in (a), (b), and (c). Note that the magnification and the contour scale are different for (d).

To compare different cases, a cumulative probability metric can be calculated by simply integrating the probability value over the domain, as follows:

$$A_{Ma>1} = \iint P_{Ma>1}(x,y) \cdot d\left(\frac{x}{c}\right) d\left(\frac{y}{c}\right) \tag{6}$$

The corresponding values of the cumulative probability ($A_{Ma>1}$) hence represent how extensive and how frequent the chances of supersonic flow are. The values are tabulated in Table 3.

4.3 Occurrence of Shock Waves

Instantaneous Schlieren images provide a clear visualization of density gradients in the flow and, hence, allow the detection of shock waves. With the current Schlieren setup, regions of the flow experiencing compression (such as shock waves), appear darker than the gray background, while flow expansion appears brighter.

From the Schlieren images, shown in Figure 8, it is straightforward to discern the presence of shock waves. At the shallowest AoA of $-4°$, no shock waves occur at the lower free-stream Mach numbers 0.5 (Figure 8a) and 0.55 (Figure 8b). However,

https://doi.org/10.5194/wes-2025-65
Preprint. Discussion started: 15 April 2025

Table 3. Cumulative probability of supersonic flow.

Case	$A_{Ma>1}$
$Ma_\infty = 0.6$, AoA$= -4^\circ$	4.70×10^{-3}
$Ma_\infty = 0.6$, AoA$= -6^\circ$	1.99×10^{-2}
$Ma_\infty = 0.6$, AoA$= -10^\circ$	2.71×10^{-2}
$Ma_\infty = 0.5$, AoA$= -10^\circ$	5.01×10^{-4}

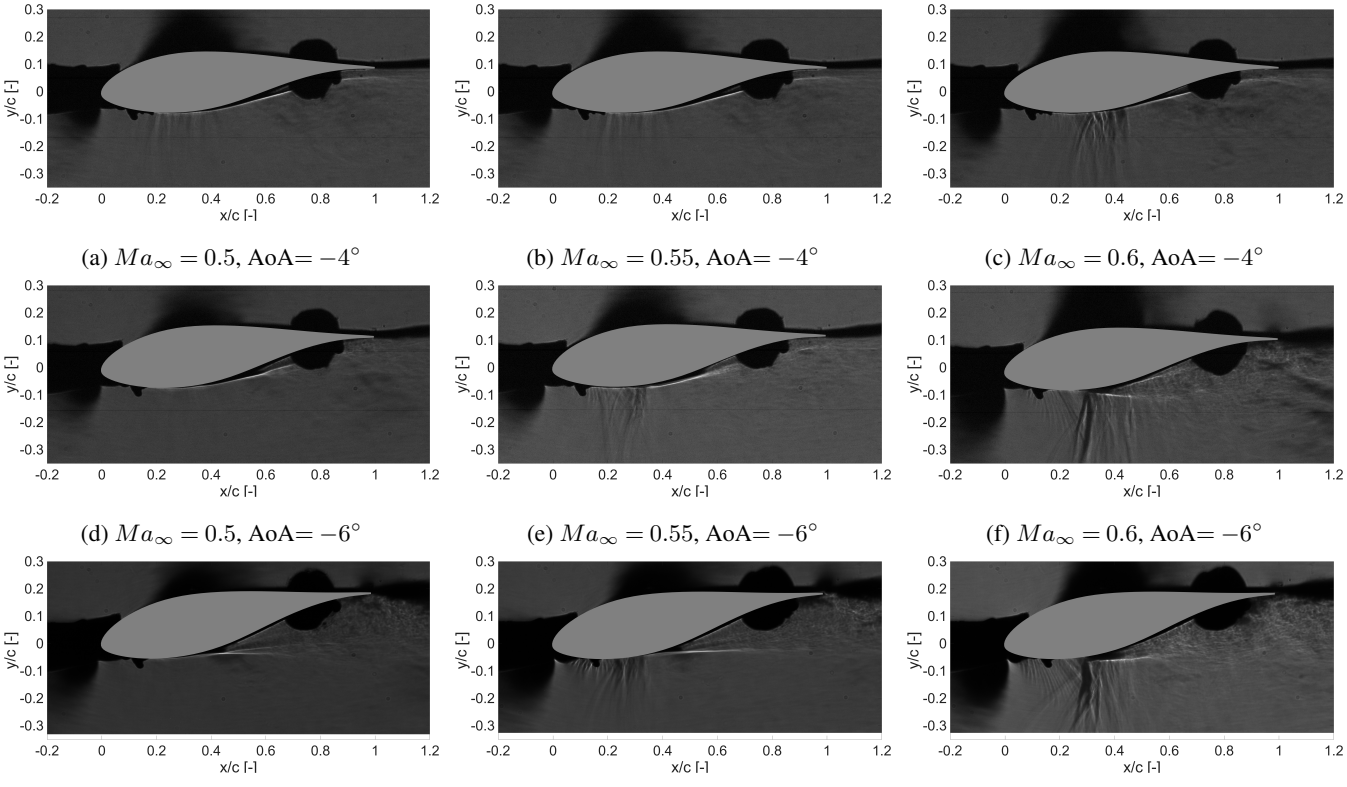

(a) $Ma_\infty = 0.5$, AoA$= -4^\circ$ (b) $Ma_\infty = 0.55$, AoA$= -4^\circ$ (c) $Ma_\infty = 0.6$, AoA$= -4^\circ$

(d) $Ma_\infty = 0.5$, AoA$= -6^\circ$ (e) $Ma_\infty = 0.55$, AoA$= -6^\circ$ (f) $Ma_\infty = 0.6$, AoA$= -6^\circ$

(g) $Ma_\infty = 0.5$, AoA$= -10^\circ$ (h) $Ma_\infty = 0.55$, AoA$= -10^\circ$ (i) $Ma_\infty = 0.6$, AoA$= -10^\circ$

Figure 8. Instantaneous Schlieren images showing the appearance of shock waves in (c), (e), (f), (h) and (i).

at $Ma_\infty = 0.6$ and AoA$= -4^\circ$, shock waves can be observed in Figure 8c. With a slightly steeper AoA of -6°, shock waves are observed for both $Ma_\infty = 0.55$ (Figure 8e) and $Ma_\infty = 0.6$ (Figure 8f), but not at $Ma_\infty = 0.5$ (Figure 8d). Similar observations are made for the steepest AoA of -10°, where $Ma_\infty = 0.5$ (Figure 8g) does not produce shock waves. This confirms that the local supersonic flow in this configuration is not adverse enough to lead to shock waves, as observed with the PIV measurements. For $Ma_\infty = 0.55$ and $Ma_\infty = 0.6$ at an AoA of -10°, shock waves can be observed in Figures 8h and 8i. In the Schlieren snapshots, multiple shocks are seen because the presence of sidewalls in the wind tunnel results in a spanwise

https://doi.org/10.5194/wes-2025-65
Preprint. Discussion started: 15 April 2025

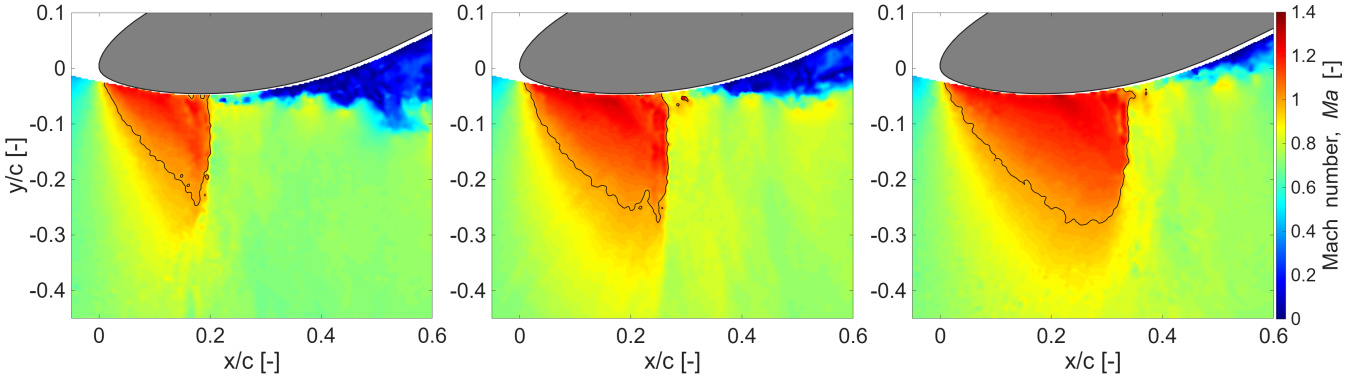

Figure 9. Instantaneous PIV frames for $Ma_\infty = 0.6$ and AoA$= -10°$. A local Mach number of 1.0 is marked with a solid black line.

With PIV, the shock front is identified more unambiguously since the measurements correspond to a single plane at the spanwise center of the model in this case. All cases discussed henceforth pertain to $Ma_\infty = 0.6$, since the earlier discussion already revealed that no shock waves were observed at $Ma_\infty = 0.5$. At an AoA of $-10°$ and $Ma_\infty = 0.6$, the shock wave also demonstrates a strongly unsteady nature, as evident from selected instantaneous Mach number contours shown in Figure 9. The shock position is observed to vary between $x/c = 0.2$ in the leftmost frame to $x/c = 0.35$ in the rightmost frame. These locations are in good agreement with the region of high standard deviation in the local Mach number ($x/c = 0.15 - 0.35$) identified as an outcome of the shock motion in Figure 6f. However, the acquisition frequency of the PIV measurements is insufficient to calculate the characteristic frequencies of the shock movement. Furthermore, the different flow field snapshots in Figure 9 give further evidence of a high unsteadiness of the separated flow region, which appears to be related to the shock motion, as commonly observed in transonic buffet studies (D'Aguanno et al., 2021).

A shock wave detection procedure is employed for the PIV snapshots (see Appendix A for details), which helps in tracking the oscillating shock wave frame-by-frame. At this low acquisition rate of the PIV data (15 Hz), subsequent PIV frames represent a random sampling of the shock motion cycle, i.e., two consecutive frames can have the shock being in completely different phases of the oscillation cycle. Also, the low acquisition rate means that the shock motion frequency, which is of a higher order, cannot be determined. Instead, a probability density function (pdf) of the shock location for different cases is calculated to gather further insight into the shock dynamics, shown in Figure 10. Here, it is worth noting that the pdf is normalized with respect to the total number of frames recorded in each case, and not by how many frames in total exhibit a shock wave. Thus, the area under each curve is representative of what percentage of time a shock wave is detected for the particular configuration.

With the shallowest AoA of $-4°$, the pdf is centered around 34% of the chord, with a total spread of $\approx 20\%$ of the chord. In comparison, when the AoA is slightly steeper at $-6°$, the pdf peak decreases and is now centered closer to 36% of the chord with a higher spread of around 25% of the chord, indicating a higher oscillation range as the transonic effects get stronger. At

https://doi.org/10.5194/wes-2025-65
Preprint. Discussion started: 15 April 2025

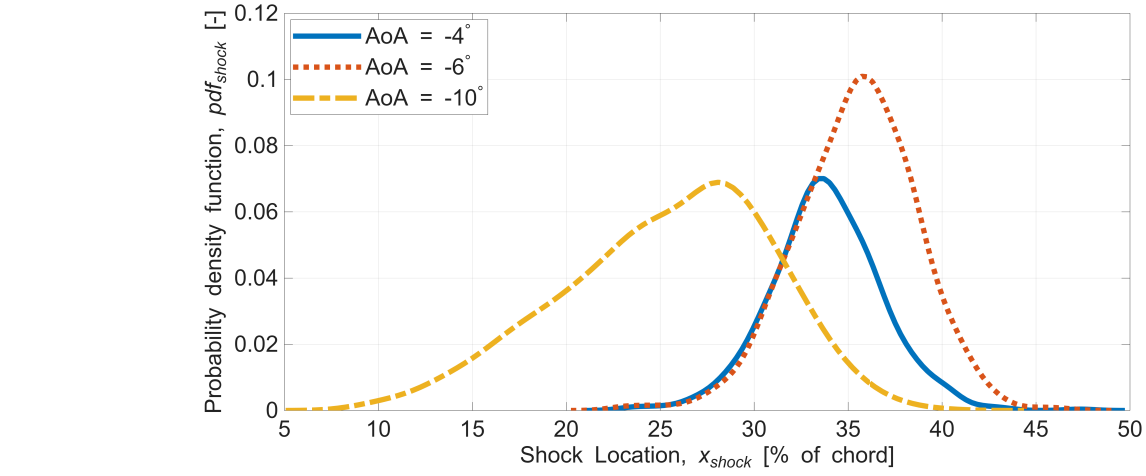

Figure 10. Probability distribution of shock locations for $Ma_\infty = 0.6$.

the steepest AoA of $-10°$, the pdf has a much lower peak and is centered more upstream, closer to 27% of the chord, with a much wider spread: 7% of the chord till 40% of the chord. This confirms that the shock motion occurs more upstream and with a greater oscillation range at the steepest AoA. Similar conclusions can be drawn by comparing the mean and standard deviations of the detected shock locations, where a steep AoA ($-10°$) results in a shock oscillating more upstream and with higher amplitude than for the shallower AoAs, as shown in Figure 10. This shift in the shock oscillation behaviour is also captured in the mean and standard deviation of the shock locations for different cases, tabulated in Table 4. A steeper AoA leads to a more upstream mean shock location and higher amplitude of oscillations for the same free-stream conditions.

Another noteworthy outcome from the shock wave detection is how frequently a shock wave is detected for the different cases. As discussed before, this can be calculated by integrating the areas under the pdfs to obtain the overall probability of shock occurrence as follows:

$$P_{shock} = \int pdf_{shock}(x) \cdot dx \tag{7}$$

In the same fashion, the overall probability of supersonic flow ($P_{Ma>1}$) can be calculated as the ratio of the number of frames that contain a minimum threshold of supersonic vectors to the total number of frames recorded. Note that this is a different measure compared to $A_{Ma>1}$ presented in section 4.2 and Table 3, which represents a probability weighted by the extent over which supersonic flow occurs. On the other hand, $P_{Ma>1}$ simply reveals how often supersonic flow is observed for a certain configuration, and the values are presented in Table 4.

It is interesting to compare the values of P_{shock} and $P_{Ma>1}$ in Table 4. For the shallowest AoA of $-4°$, supersonic flow occurs 97% of the time, however, shock waves are detected only in 48% of the frames. The intermittency in shock occurrence is illustrated in Figure 11, where three instantaneous frames for $Ma_\infty = 0.6$ and AoA$= -4°$ are shown, and the local supersonic pocket is marked with a solid black line. The left and middle frames are seen to contain supersonic flow pockets, but these are small and do not terminate abruptly so as to indicate a shock. However, the right frame contains a relatively larger local

https://doi.org/10.5194/wes-2025-65
Preprint. Discussion started: 15 April 2025

eawe european academy of wind energy
Open Access WIND ENERGY SCIENCE DISCUSSIONS

Table 4. Characteristic properties of shock occurrence at $Ma_\infty = 0.6$.

Case	Mean x_{shock} [% of chord]	Std. dev. x_{shock} [% of chord]	P_{shock} [%]	$P_{Ma>1}$ [%]
AoA$= -4^\circ$	33.8	3.0	48	97
AoA$= -6^\circ$	35.3	3.2	79	100
AoA$= -10^\circ$	25.3	5.5	95	100

supersonic region, which culminates in a shock wave, as suggested by the vertical shape of the downstream edge of the supersonic pocket.

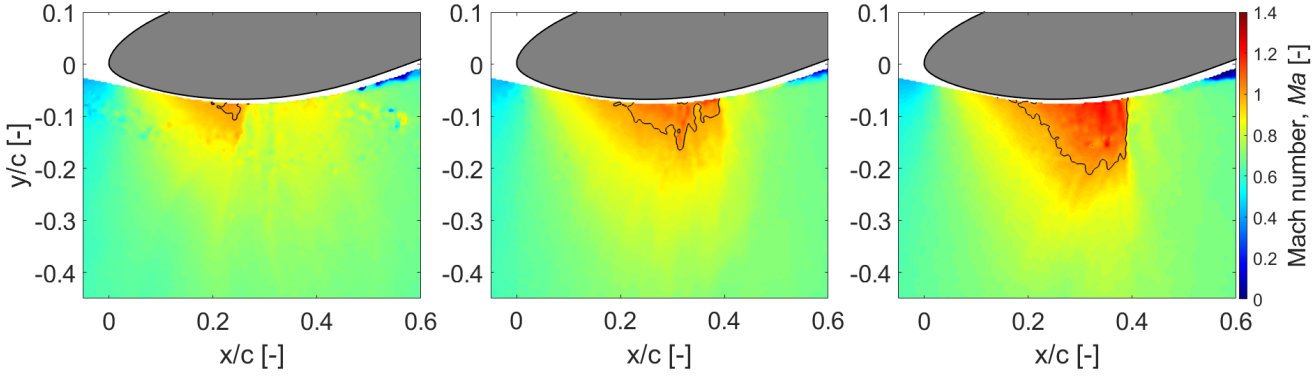

Figure 11. Instantaneous PIV frames for $Ma_\infty = 0.6$ and AoA$= -4^\circ$. A local Mach number of 1.0 is marked with a solid black line. All three frames show a local supersonic flow region, but only the rightmost frame contains a shock (at $x/c \approx 0.4$).

For the two steeper AoAs, supersonic flow always occurs. However, for AoA$= -6^\circ$, shock waves are observed around 79% of the time, whereas for the steepest inclination of -10°, 95% of the frames exhibit shock waves. Thus, the occurrence of supersonic flow is not a guarantee of a shock wave forming, especially for shallower AoAs where shock wave occurrence could be intermittent rather than consistent. In wind turbine operation, intermittent shock waves at AoA$= -4^\circ$ will lead to much different loading compared to steeper AoAs, where shock waves might always be present but with a large range of oscillation.

5 Discussion

For the higher Ma_∞ of 0.6, the PIV experiments confirmed that shock waves occurred at all AoAs investigated: -4°, -6°, and -10°. The latter two conditions were predicted to exhibit supersonic flow according to Figure 4, while the former case was not. The presence of oscillating shock waves was reflected in the mean and standard deviation of the local Mach number fields for each of the aforementioned cases. When Ma_∞ was lowered to 0.5 for an AoA of -10°, a condition predicted to experience local supersonic flow in Figure 4, no shock waves were observed! Furthermore, only a considerably tiny region (around 5%

https://doi.org/10.5194/wes-2025-65
Preprint. Discussion started: 15 April 2025

eawe european academy of wind energy
Open Access WIND ENERGY SCIENCE DISCUSSIONS

of the chord in extent) was seen to exhibit supersonic flow intermittently: only 1/3 of the time, at maximum. In contrast, local supersonic flow occurred more consistently over a significantly greater extent in all the $Ma_\infty = 0.6$ cases, as seen in Figure 7. These observations highlight the limitations of the transonic envelope calculations based on theory and low-fidelity modelling, mainly the inability to predict the frequency and intensity of transonic flow effects.

Likely, for $Ma_\infty = 0.5$, the suction peak was not strong enough to cause a sufficient flow acceleration to produce larger regions of supersonic flow and eventually shock waves. This could be due to an effective de-cambering of the airfoil at the given AoA of $-10°$ following a large separation of the boundary layer. However, this de-cambering effect is not equally effective when the free-stream Mach number is raised to 0.6 for the same AoA of $-10°$, as flow accelerates sufficiently to result in shock waves. However, flow separation was not explicitly analyzed for any of the cases. Thus, the calculation of the transonic envelope presented in Figure 4 is not sufficient to predict the occurrence of shock waves.

The Mach number effects were identifiable in the Schlieren visualizations (Figure 8) leading to shock waves growing in strength with an increase in free-stream Mach number at the same inclination. The unsteady nature of the shock waves was also established both qualitatively: through studying instantaneous PIV snapshots, and quantitatively: by tracking the shock location in the PIV frames. While spectral analysis could not be carried out to determine the characteristic frequencies of the shock oscillation, the sensitivity of the extent and severity of shock wave oscillations was evident from the probability density functions of the shock location. Also, the steepness of the AoA plays a vital role in determining whether shock waves occur intermittently ($\sim 48\%$ of the time for AoA$= -4°$) or consistently ($\sim 95\%$ of the time for AoA$= -10°$). For the former case, it was also observed that supersonic flow occurred 97% of the time. However, it does not lead to shock waves as often. In either case, the intermittent and unsteady nature of shock waves would pose a problem through increased fatigue loading and the possibility of resonance with the structure if they were to occur on wind turbine blades.

The primary limitation of this study is that the free-stream Mach number range studied here is beyond the expected operational range of large wind turbines at present. The largest wind turbine designed, IEA 22MW RWT, experiences a free-stream Mach number of 0.3 at the tip. While there is a negligible possibility for wind turbines in the near future to operate at higher free-stream Mach numbers of 0.5 and above at the tip, it is still useful to study the aerodynamics of the tip airfoil at these conditions. Firstly, it helped us identify the lower limit at which we can expect shock waves. Thus, we can already consider current wind turbines to be safe from the detrimental consequences of shock wave occurrence, since they first start appearing at much higher free-stream Mach numbers than current operational limits. Secondly, it allowed us to validate and identify the drawbacks of low-fidelity modelling to predict transonic flow on highly cambered airfoils, highlighting the complex interactions that may escape low-order capabilities. It is possible that at conditions closer to $Ma_\infty = 0.3$ and AoA of $-15°$, where the IEA 15MW and 22MW RWT blade tip is predicted to experience the transonic regime by De Tavernier and von Terzi (2022), the flow physics might turn out to be surprisingly unique.

Another important factor to be taken into account is the Reynolds number of the flow. In the current study, the Reynolds number is of the order of 1×10^6, and it is expected to be an order of magnitude higher for tip airfoils on actual wind turbines of the largest scale. This discrepancy was shown, through URANS simulations by Vitulano et al. (2025), to exacerbate the extent and severity of local supersonic flow pockets at a higher Reynolds number for the same combination of Ma_∞ and AoA lying

https://doi.org/10.5194/wes-2025-65
Preprint. Discussion started: 15 April 2025

eawe european academy of wind energy
Open Access WIND ENERGY SCIENCE DISCUSSIONS

beyond the transonic envelope. In short, it makes the transonic envelope shift to lower Ma_∞ for the same AoA, with a more pronounced shift at higher AoAs. Thus, it can be expected that under actual operating conditions (with significantly higher Reynolds numbers), the safety margin with respect to experiencing transonic flow and shock waves at wind turbine tips might be shorter than observed in the current experiments. Transonic flow and shock waves might occur under less severe conditions of the Ma_∞ and AoA. However, due to practical constraints on the experimental facility utilized, it is not possible to increase the Reynolds number by an order of magnitude and verify this experimentally.

6 Conclusions

Basic isentropic flow theory combined with low-fidelity airfoil design tools such as XFoil allows us to predict what combinations of free-stream Mach number and AoA lead to transonic flow over a static FFA-W3-211 airfoil, as depicted in Figure 4. While these calculations indicate when to expect transonic flow in a binary sense, they are not capable of predicting the frequency and intensity of the supersonic flow features, especially the appearance of shock waves. The current study shows that there exist substantial disparities in terms of how transonic effects manifest for different configurations. This added complexity is not accounted for by the transonic envelope calculations, warranting a more comprehensive characterization of airfoil behavior in transonic flow regimes with higher fidelity simulation techniques or a combination of experiments and state-of-the-art simulations.

Through Schlieren images, it was seen that, for the Reynolds numbers studied here, shock waves start to appear at $Ma_\infty = 0.55$. For $Ma_\infty = 0.5$, tiny supersonic flow pockets might exist (as captured using PIV) at steep inclinations ($-10°$) but are not adverse enough to culminate in shock waves, unlike at higher Ma_∞. Shock wave occurrence was analyzed in depth through PIV measurements at $Ma_\infty = 0.6$, displaying an inherently unsteady behaviour. While all configurations tested at $Ma_\infty = 0.6$ consistently had significant regions of supersonic flow, the frequency of occurrence of shock waves was seen to vary from intermittent to nearly omnipresent as the airfoil inclination was steepened. In general, the steeper the inclination, the higher the likelihood of shock waves for the same Ma_∞. Additionally, a steeper inclination also translates to shock waves appearing more upstream as well as having a broader oscillation range at a given Ma_∞.

In real-world operating conditions, the inherent unsteadiness of the oncoming wind and dynamic pitching of the blades to optimize loads in response to the wind means that Ma_∞ and AoA are never static on a wind turbine airfoil. Thus, the scope of future studies includes testing the airfoil under dynamic inflow conditions.

Data availability. The processed PIV data and post-processing code are openly accessible here: doi.org/10.4121/fbf1c251-cbf9-49d7-9626-a9fe3498aed5.
(NOTE: This link will become active after the paper is accepted for publication.)

https://doi.org/10.5194/wes-2025-65
Preprint. Discussion started: 15 April 2025

eawe european academy of wind energy
Open Access WIND ENERGY SCIENCE DISCUSSIONS

Appendix A: Shock Detection Methodology

While visualizing shock waves qualitatively is relatively straightforward with Schlieren and instantaneous PIV frames, detecting them quantitatively is more demanding. In this section, the methodology developed to detect shock wave locations from instantaneous PIV measurements is discussed. The underlying assumption is that the shock wave is always normal to the free-stream direction, which is a reasonable estimation given that only slight deviations are occasionally observed. The sequence of operations used to confirm the presence of a shock and, if present, detect its location in each PIV frame is listed below:

1. Detect the points of maximum gradient in streamwise velocity in a specified region of the PIV frame. All subsequent operations are carried out with reference to these points.
2. From the points detected in the previous operation, eliminate the points that do not have any supersonic flow vectors close upstream or have supersonic flow close downstream.
3. Perform a zeroth-order fit on (i.e., find the mean of) the streamwise locations (x locations, in this case) of the remaining points.
4. Remove the points that are 1.5 standard deviations (chosen based on trial-and-error) away from the mean calculated above, to reinforce the normal shock orientation assumption.
5. If the standard deviation of the remaining points is beyond a specified threshold, or the number of remaining points is beneath a specified limit, then reject the case (i.e., no shock detected).

Shock waves are characterized by strong gradients in the flowfield, but additional constraints need to be applied to ascertain their location. This includes checking the presence of supersonic flow upstream and subsonic flow downstream, to ensure that the detection of points of highest gradients (in velocity, in this case) corresponds to the expected location of the shock front. In cases when the appearance of shocks is intermittent and supersonic flow can sometimes gradually decelerate without resulting in a shock, the additional filtering using the standard deviation in steps 4 and 5 helps in avoiding erroneously observing a shock when there is none.

Some examples of the shock detection methodology in action are presented next. Note that the direction of flow is from left to right. In Figure A1, the leftmost figure shows the points (as magenta squares) that have the maximum gradient in streamwise velocity at respective transverse locations. A few points towards the bottom lie inside the supersonic flow pocket (marked with a solid black line) rather than on its downstream edge, as expected for a shock front. As seen in the middle frame, these points are eliminated after checking for supersonic flow upstream (which holds true) and subsonic flow downstream (which is violated). Finally, as seen in the right frame, the final detected shock location is marked with a dashed black line after performing the checks regarding the standard deviation on the remaining points.

Another example is presented in Figure A2, where it is already expected that no shock wave is present. The supersonic upstream/subsonic downstream check (shown in the middle frame) takes care of almost all the potential shock front points detected by the maximum streamwise velocity gradient (left), except for a few next to a tiny supersonic pocket at $x/c \approx 0.2$.

https://doi.org/10.5194/wes-2025-65
Preprint. Discussion started: 15 April 2025

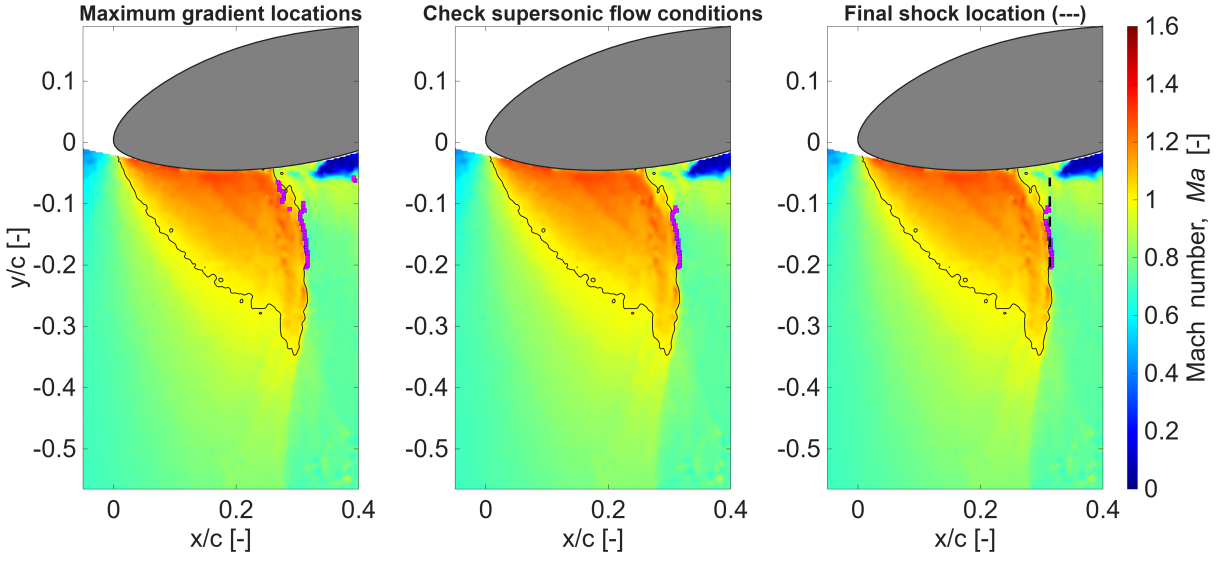

Figure A1. Instantaneous local Mach number field for $Ma_\infty = 0.6$, AoA$= -10^\circ$ with local supersonic flow pocket (marked with solid black line), detected shock locations (magenta markers) and the final shock front location (dashed black line) on the right.

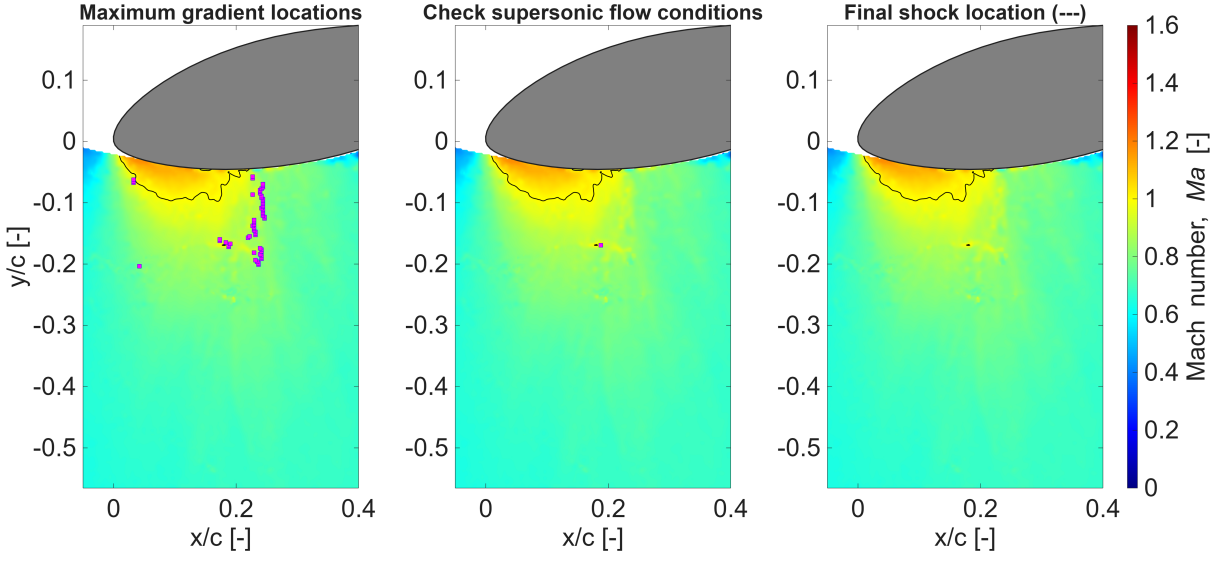

Figure A2. Instantaneous local Mach number field for $Ma_\infty = 0.6$, AoA$= -10^\circ$ with local supersonic flow pocket (marked with solid black line) and detected shock locations (magenta markers). No shock front is detected after the filtering process, as seen on the right.

The next filtering step, based on the number of remaining points and the standard deviation, eliminates the last few detected points as well, rightly resulting in no shock front detected for the case.

https://doi.org/10.5194/wes-2025-65
Preprint. Discussion started: 15 April 2025

eawe european academy of wind energy
Open Access WIND ENERGY SCIENCE DISCUSSIONS

Author contributions. AA was responsible for the overall research, under the supervision of DDT, FS, BvO, and DvT. AA carried out the experimental measurements as well as the post-processing of the measurements with the support of FS and BvO. The results were visualized by AA and analyzed by AA, DDT, FS, BvO, and DvT. The underlying data of Figure 4 was generated by simulations carried out by DDT. The first draft was prepared by AA, and subsequent corrections were made according to the reviews by DDT, FS, BvO, and DvT.

Competing interests. The authors declare that they have no conflict of interest.

https://doi.org/10.5194/wes-2025-65
Preprint. Discussion started: 15 April 2025

eawe european academy of wind energy
Open Access WIND ENERGY SCIENCE DISCUSSIONS

References

Benedict, L. and Gould, R.: Towards better uncertainty estimates for turbulence statistics, Experiments in Fluids, 22, 129–136, 1996.

Bertagnolio, F., Sørensen, N. N., Johansen, J., and Fuglsang, P.: Wind turbine airfoil catalogue, 2001.

De Kat, R. and Van Oudheusden, B.: Instantaneous planar pressure determination from PIV in turbulent flow, Experiments in Fluids, 52, 1089–1106, 2012.

De Tavernier, D. and von Terzi, D.: The emergence of supersonic flow on wind turbines, in: Journal of Physics: Conference Series, vol. 2265, p. 042068, IOP Publishing, 2022.

D'Aguanno, A., Schrijer, F., and van Oudheusden, B.: Experimental investigation of the transonic buffet cycle on a supercritical airfoil, Experiments in Fluids, 62, 1–23, 2021.

Herriot, J. G.: Blockage corrections for three-dimensional-flow closed-throat wind tunnels, with consideration of the effect of compressibility, Tech. rep., 1947.

Hossain, M. A., Huque, Z., and Kammalapati, R. R.: Propagation of shock on NREL phase VI wind turbine airfoil under compressible flow, Journal of Renewable Energy, 2013, 653 103, 2013.

Humble, R.: Unsteady Flow Organization of A Shock Wave/Boundary Layer Interaction, Dissertation, Delft University of Technology, Netherlands, ISBN 978-90-597-2295-8, 2009.

Mehta, M., Zaaijer, M., and von Terzi, D.: Drivers for optimum sizing of wind turbines for offshore wind farms, Wind Energy Science, 9, 141–163, 2024a.

Mehta, M., Zaaijer, M., and von Terzi, D.: Designing wind turbines for profitability in the day-ahead markets, Wind Energy Science, 9, 2283–2300, 2024b.

Schrijer, F. and Scarano, F.: Effect of predictor–corrector filtering on the stability and spatial resolution of iterative PIV interrogation, Experiments in Fluids, 45, 927–941, 2008.

Vitulano, M. C., De Tavernier, D., De Stefano, G., and von Terzi, D.: Numerical analysis of transonic flow over the FFA-W3-211 wind turbine tip airfoil, Wind Energy Science, 10, 103–116, https://doi.org/10.5194/wes-10-103-2025, 2025.

Wood, D.: Some effects of compressibility on small horizontal-axis wind turbines, Renewable Energy, 10, 11–17, 1997.

Zahle, F., Barlas, T., Lonbaek, K., Bortolotti, P., Zalkind, D., Wang, L., Labuschagne, C., Sethuraman, L., and Barter, G.: Definition of the IEA Wind 22-Megawatt Offshore Reference Wind Turbine, Tech. rep., National Renewable Energy Laboratory (NREL), Golden, CO (United States), 2024.